JGR Space Physics

RESEARCH ARTICLE
10.1029/2021JA029286

Key Points:

- S0 and W1 quasi-10 day planetary waves (Q10DWs) were forced during the 2019 Southern sudden stratospheric warming (SSW), possibly through Q10DW-E1 nonlinear interactions with stationary planetary waves
- Latitudinal structures of stratospheric Q10DWs are similar to those expected based on solutions to Laplace's tidal equation
- The Q10DWs couple the neutral atmosphere and ionosphere during the 2019 Antarctica SSW

Supporting Information:

Supporting Information may be found in the online version of this article.

Correspondence to:

J. C. Wang,
jack.c.wang@colorado.edu

Citation:

Wang, J. C., Palo, S. E., Forbes, J. M., Marino, J., Moffat-Griffin, T., & Mitchell, N. J. (2021). Unusual quasi 10-day planetary wave activity and the ionospheric response during the 2019 Southern Hemisphere sudden stratospheric warming. *Journal of Geophysical Research: Space Physics*, *126*, e2021JA029286. https://doi.org/10.1029/2021JA029286

Received 25 FEB 2021
Accepted 26 MAY 2021

Unusual Quasi 10-Day Planetary Wave Activity and the Ionospheric Response During the 2019 Southern Hemisphere Sudden Stratospheric Warming

J. C. Wang[1,2], S. E. Palo[1], J. M. Forbes[1], J. Marino[1], T. Moffat-Griffin[3], and N. J. Mitchell[3,4]

[1]Ann and H.J. Smead Department of Aerospace Engineering Sciences, University of Colorado Boulder, Boulder, CO, USA, [2]High Altitude Observatory, National Center for Atmospheric Research, Boulder, CO, USA, [3]British Antarctic Survey, Cambridge, UK, [4]Department of Electronic and Electrical Engineering, University of Bath, Bath, UK

Abstract An unusual sudden stratospheric warming (SSW) event occurred in the Southern Hemisphere in September 2019. Ground-based and satellite observations show the presence of transient eastward- and westward-propagating quasi-10 day planetary waves (Q10DWs) during the SSW. The planetary wave activity maximizes in the mesosphere and lower thermosphere region approximately 10 days after the SSW onset. Analysis indicates that the westward-propagating Q10DW with zonal wave number $s = 1$ is mainly symmetric about the equator, which is contrary to theory which predicts the presence of an antisymmetric normal mode for such planetary wave. Observations from microwave limb sounder and sounding of the atmosphere using broadband emission radiometry are combined with meteor radar wind measurements from Antarctica, providing a comprehensive view of Q10DW wave activity in the Southern Hemisphere during this SSW. Analysis suggests that the Q10DWs of various wavenumbers are potentially excited from nonlinear wave-wave interactions that also involve stationary planetary waves with $s = 1$ and $s = 2$. The Q10DWs are also found to couple the ionosphere with the neutral atmosphere. The timing of the quasi-10-day oscillations (Q10DOs) in the ionosphere are contemporaneous with the Q10DWs in the neutral atmosphere during a period of relatively low solar and geomagnetic activity, suggesting that the Q10DWs play a key role in driving the ionospheric Q10DOs during the Southern SSW event. This study provides observational evidence for coupling between the neutral atmosphere and ionosphere through the upward propagation of global scale planetary waves.

Plain Language Summary Sudden stratospheric warmings (SSWs) are a common dynamical feature in the Northern Hemisphere, but they rarely happen in the Southern Hemisphere because of weaker planetary wave activity due to smaller land/sea thermal differences. In September 2019, a record-strong SSW was observed in the Southern Hemisphere, accompanied by the amplification of traveling planetary waves with a period near 10 days during the onset of this Southern Hemisphere SSW. Analysis suggests that the quasi 10-day planetary waves can drive the quasi-10-day oscillations in the ionosphere. Our result suggests the amplification of the quasi 10-day planetary waves during SSWs can make significant impacts on the upper atmosphere.

1. Introduction

Sudden stratospheric warmings (SSWs) refer to rapid warming events in the polar stratosphere, which usually occur during mid-winter (Andrews et al., 1987). These large-scale phenomena are triggered by enhancement of vertically propagating quasi-stationary planetary waves (QSPWs) (Labitzke, 1981) generated in the troposphere by land-sea thermal differences and/or large-scale topography. The breaking of QSPWs in the polar stratosphere can disrupt the wintertime polar vortex and affect the mean circulation (Matsuno, 1971). The polar vortex can either be displaced and/or split due to the forcing from the breaking of QSPWs. To this extent, in the polar stratosphere the background eastward wind would be decelerated and the temperature can increase tens of K very rapidly. This aspect of stratospheric dynamics is the key driver of the SSWs and can impact the dynamics of the upper atmosphere (Gan et al., 2020; Goncharenko et al., 2010; Limpasuvan et al., 2016; Liu & Roble, 2005; Mo & Zhang, 2020; Pancheva et al., 2008; Pedatella & Liu, 2013; Siskind et al., 2005; Yamazaki et al., 2020).

Although SSWs are common features during Arctic winter, they are rare in the Antarctic (Chandran et al., 2014) because of weaker land/sea thermal difference and orographic forcing (Andrews et al., 1987; Chandran et al., 2014; van Loon et al., 1973). A notable exception was observed in September 2002 (Allen et al., 2003), being the only major SSW event in the Southern Hemisphere over past eight decades of observation (Chandran et al., 2014; Krüger et al., 2005). A major SSW event is associated with a reversal of the temperature gradient at 10 hPa poleward of 60° latitude, accompanied by a reversal of the mean zonal wind from eastward to westward at or below 10 hPa and 60° latitude. A minor SSW refers to a reversal of temperature gradient without the reversal of the zonal wind (Butler et al., 2015). Analysis of the 2002 Southern SSW has shown that the wave interaction between the QSPWs, quasi 10-day propagating planetary waves (Q10DWs) and background atmospheric state play a major role in pre-conditioning the atmosphere before the onset of a SSW event (Krüger et al., 2005; Palo et al., 2005). In that event, robust growth of Q10DWs also perturbed the ionosphere and drove an apparent quasi 10-day oscillation (Q10DO) of total electron content (TEC) in the equatorial ionospheric anomaly (EIA) crest region (Mo & Zhang, 2020).

The westward-propagating Q10DW with zonal wave number one (Q10DW-W1) exists as a force-free normal mode (NM) oscillation in the middle atmosphere, as the classical wave theory on a spherical-rotating Earth predicts (Forbes, 1995). Observations have shown that the Q10DW-W1 has distinct seasonal behavior with its minimum usually located in the summer hemisphere (Forbes & Zhang, 2015). The latitudinal structure matches well with theoretical prediction in the middle atmosphere (Forbes & Zhang, 2015), which is antisymmetric about the equator (Forbes, 1995). The large amplitude of Q10DW-W1 has also been observed during final warmings (Yamazaki & Matthias, 2019; Yu et al., 2019). Note that stratospheric warming events are considered to be final warmings when the polar vortex breaks down, and the mean zonal wind reverses from eastward to westward without a subsequent eastward reversal until the following autumn (Butler et al., 2017). The amplification of Q10DW-W1 is attributed to the enhanced atmospheric instability during final warmings which could excite and amplify the NM.

In September 2019, the Southern Hemisphere stratosphere experienced a strong SSW event beginning on August 25, 2019 (Lim et al., 2020). Strictly, the conditions for a major SSW were not met since the zonal mean zonal wind at 10 hPa and 60°S latitude did not undergo a reversal. However, the magnitudes of the zonal mean zonal wind and temperature changes were comparable to those of the 2002 SH major SSW. The changes of polar cap temperature at 30 hPa were reported to be the strongest warming on record for September over 40 years of satellite observations (Lewis, 2019; Lim et al., 2020). This offers a unique opportunity to revisit current understanding of lower and upper atmospheric coupling mechanisms through the amplification of planetary waves during SSWs in the Southern Hemisphere.

In this study, a rapid growth of QSPWs along with Q10DWs are reported. The Q10DW-W1 was found to be a symmetric mode in the middle atmosphere. This result is contrary to the classical theory of atmospheric waves which predicts the Q10DW-W1 is expected to be an antisymmetric (1,−3) NM (Forbes, 1995; Hough, 1898). Observations from ground-based and space-based instruments have demonstrated evidence of coupling between the lower and upper atmosphere through enhanced planetary wave activity during the 2019 Southern SSW. Ionospheric observations show a quasi 10-day periodicity in the EIA region. Our analysis indicates that Q10DWs play an important role in ionospheric variability during 2019 Southern Hemisphere SSW event, and that planetary waves can effectively couple the troposphere to the ionosphere.

2. Data and Methodology

2.1. Meteor Radars

Vector winds measured by meteor radars located at McMurdo Station (77°51′S, 166°40′E) and Rothera Research Station (67°34′S, 68°07′W) (Sandford et al., 2010) in the Antarctic are utilized in this study. Meteor radars are sensitive to the backscatter from the ionization deposited from the ablation of meteoroids in the atmosphere. This plasma is advected with the motion of the ambient neutral wind fields in the mesosphere and lower thermosphere (MLT) (Elford & Robertson, 1953; Robertson et al., 1953). This type of ground-based meteor radar system statistically combines a number of individual measurements, yielding estimates of the hourly mean wind fields in the MLT.

Both the McMurdo and Rothera meteor radars are SKiYMET-type systems as described in Hocking et al. (2001). In general, these systems are pulsed coherent radars operating in the VHF (very high frequency) range, with interferometric receiving arrays that allow determination of unambiguous angle-of-arrival. These radars typically produce hourly mean zonal and meridional wind components between the altitudes of 82 and 98 km in overlapping 4 km bins centered at 82, 85, 88, 91, 94, and 98 km. On average, based on the number of meteors available and intrinsic uncertainty of their radial velocities, the uncertainty of the hourly wind estimations is about ∼5 ms^{-1}. Details for the Rothera system can be found in (Sandford et al., 2010).

2.2. Sounding of the Atmosphere Using Broadband Emission Radiometry

The thermosphere-ionosphere-mesosphere energetics and dynamics (TIMED) satellite was designed to investigate the dynamical and chemical processes in the MLT and ionosphere (Yee et al., 1999). The spacecraft was launched on December 7, 2001, into a 74-degree inclination, 625 ± 25 km circular, quasi-sun-synchronous orbit. The sounding of the atmosphere using broadband emission radiometry (SABER) experiment (Dawkins et al., 2018; Russell et al., 1999) on TIMED is one of four instruments onboard the spacecraft. The SABER instrument is a limb scanning radiometer that measures vertical radiance profiles with 10 spectral channels that span 1.27-μm to 17-μm. The kinetic temperature is retrieved from the measured 15-μm CO_2 radiance with a forward model using monthly and diurnally averaged CO_2 profiles from the Whole Atmosphere Community Climate Model (Remsberg et al., 2008). The retrieved temperature profiles cover latitudes between 53°N–82°S and 82°N–53°S with a 60–63 day periodicity depending on the yaw mode of the spacecraft, at altitudes from 10 to 120 km with ∼2 km resolution. In this study, SABER version 2.0 (http://saber.gats-inc.com) temperature observations within ±50° latitude are utilized to obtain the wave structures, and the uncertainty of the product is summarized in Table S1 in the supporting material. Note that we limit our analysis to ±50° latitude for SABER data because the measurements can continuously cover in Universal Times (UTs) and longitudes without interruption by the yaw maneuvers.

Because the TIMED spacecraft is in a slowly precessing orbit, the local time of each profile over the same latitude circle is approximately constant over one day. Taking the ascending and descending measurements together, roughly 60 days are required to make measurements covering 24 h of solar local time. Following the procedure implemented in Forbes and Zhang (2015) and Forbes, Zhang, et al. (2018), 60-day averaged tides are removed from the raw data before obtaining the PW amplitudes and phases. This tidal-removed residual is calculated using a 60 day window that moves forward 1 day at a time. The PW amplitudes and phases are then determined from least squares fits to the residuals in 5° latitude bins extending from 50°S to 50°N latitude. Within each window, fits are performed to periods ranging from 3.0 to 20.0 days in increments of 0.125 days, the analysis windows are 3 times the wave period, and the zonal wave numbers span from −2 to 2. Negative wave number indicate westward propagation.

2.3. Microwave Limb Sounder

The microwave limb sounder (MLS) (Waters et al., 2006) was launched onboard the Earth Observing System (EOS) Aura spacecraft (Schoeberl et al., 2006) on July 15, 2004. Aura is a member of the Afternoon Constellation, designed to observe changes in atmospheric composition along with several other Earth-observing satellites in the same orbital track. The EOS Aura spacecraft is in a 705-km sun-synchronous polar orbit (98° inclination) with a 1:45 p.m. ascending equatorial crossing time. MLS makes limb sounding observing during both day and night, using heterodyne radiometers that measure the thermal emission in 5 spectral channels (118, 190, 240, 640 GHz, and 2.5 THz).

The geopotential height product (GPH) is retrieved primarily from the 118- and 234-GHz O_2 line emissions, covering latitudes from 82°S to 82°N, and altitudes from 261 to 1×10^{-3} hPa (∼10 to 95 km). Note that in the remainder of the paper the vertical pressure coordinates are converted into the approximate geometric heights and the results are reported using this approximate height. The vertical resolution of the MLS GPH is not regular, and ranges from ∼4.5 km in the stratosphere to ∼10 km in the mesosphere (Livesey et al., 2017). The along-track resolution is ∼165 km in the stratosphere and decreases to ∼280 km in the mesosphere. Version 4.2 MLS level 2 GPH product is used in this study. The estimated precision of the GPH product is 20–25 m below 1 hPa (∼48 km), and degrades to 110 m at 0.01 hPa (∼80 km) (Livesey et al., 2017).

Following the procedure in Yamazaki and Matthias (2019), the daily mean value at each latitude circle and orbit node is independently subtracted from the raw data before computing the PW structure. This approach reduces the potential aliasing from the migrating tides into the PW fits. The PW amplitudes and phases are then determined from this residual using a least squares fit. The fits are performed similar to those described for the TIMED SABER data.

2.4. COSMIC-2/Global Ionosphere Specification

The Global ionosphere specification (GIS) is a novel ionospheric assimilation product which provides global coverage of the hourly electron density distribution from heights of 100–1,000 km with a vertical resolution of 20 km, and a geographic latitude/longitude resolution of 2.5° × 5° (C. Y. Lin et al., 2015, 2017, 2020). To form this global distribution of electron density, slant TEC observations from ground-based Global Positioning System receivers and radio occultation receivers onboard FORMOSAT-7/COSMIC-2 are assimilated into the nowcast model by implementing a Gauss-Markov Kalman filter algorithm (C. Y. Lin et al., 2017). The GIS products have been validated by comparison with ground-based observations (C. Y. Lin et al., 2020) and have been utilized to investigate atmosphere-ionosphere coupling via vertical propagation of PWs during 2019 SSW (J. T. Lin et al., 2020). The GIS products utilized in this study are transformed into apex magnetic coordinates using the International Geomagnetic Reference Field (Finlay et al., 2010).

Previous studies were used to obtain the ionospheric PW-like oscillation in a fixed local time frame (e.g., J. T. Lin et al., 2020; Yamazaki, 2018; Yamazaki et al., 2020), and found that the observed ionospheric oscillations associated with the vertically propagating waves show distinct local time dependence. However, this method is not efficient to resolve the response due to the global-scale atmospheric waves propagating from the MLT, which have coherent structures in time and longitude. In this study a fitting method that was developed for MLT wave studies is implemented. That is, for this approach the PW amplitudes and phases are estimated using a least squares fits to the data from grid points at all available longitudes and UTs but at a constant latitude. This method has been applied previously to atmosphere-ionosphere coupling studies and has been demonstrated to resolve signatures of global-scale PWs and tides in the ionosphere due to waves propagating upwards from the MLT region (Chang et al., 2011; Pedatella & Forbes, 2010). Similar to the neutral atmosphere analysis, fits are performed to periods ranging from 3 to 20 days in increments of 0.125 days, but over analysis windows that are five times the wave period to provide a narrower bandwidth and better resolve the spectral complexity of the wave activity in the ionosphere. The zonal wave numbers used for this analysis span from −2 to 2.

3. Results

3.1. Quasi 10-Day Planetary Waves in the Neutral Atmosphere

Figures 1a and 1b show the Morlet wavelet spectra (Torrence & Compo, 1998) for the meridional wind at 91 km height measured by the meteor radars at McMurdo and Rothera stations, respectively. It can be clearly seen that a transient 8–11 day periodicity, centered near 9 days, is present at the onset of the 2019 SSW at both stations. The power of the signal reaches 180 m^2/s^2 at both stations around day 248, the onset of the SSW, and gradually decreases thereafter. In our analysis, the dominant wave number is resolved through phase-differencing by cross-wavelet analysis between the two stations (He et al., 2018). Such a technique is valid when applied to a wave in which only a single component presents at any given frequency, and the meridional phase variation of that wave component is negligible. The cross-wavelet spectrum between McMurdo and Rothera stations is shown in Figure 1c, suggesting that the dominant wave number is one and the planetary wave is westward propagating ($m = -1$). The results are consistent with observations of the Q10DW in the Northern Hemisphere (He et al., 2020) and at King Sejong Station (62.22°S, 58.78°W) (Eswaraiah et al., 2020) during the 2019 Southern SSW, indicating the Q10DW is a global scale feature.

To better understand the global response of the Q10DW during the 2019 Southern SSW, and to determine if it exhibits NM behavior, the MLS GPH and SABER temperature measurements are analyzed. Figure 2 shows the MLS GPH spectrum of westward propagating waves with zonal wave number one ($m = -1$) as a function of period and geographic latitude at a height of 92 km. The dominance of wave periods near 6 and 8–9 days suggests the presence of the Q6DW and Q10DW. The Q10DW (Q6DW) maximizes at ±40–50°

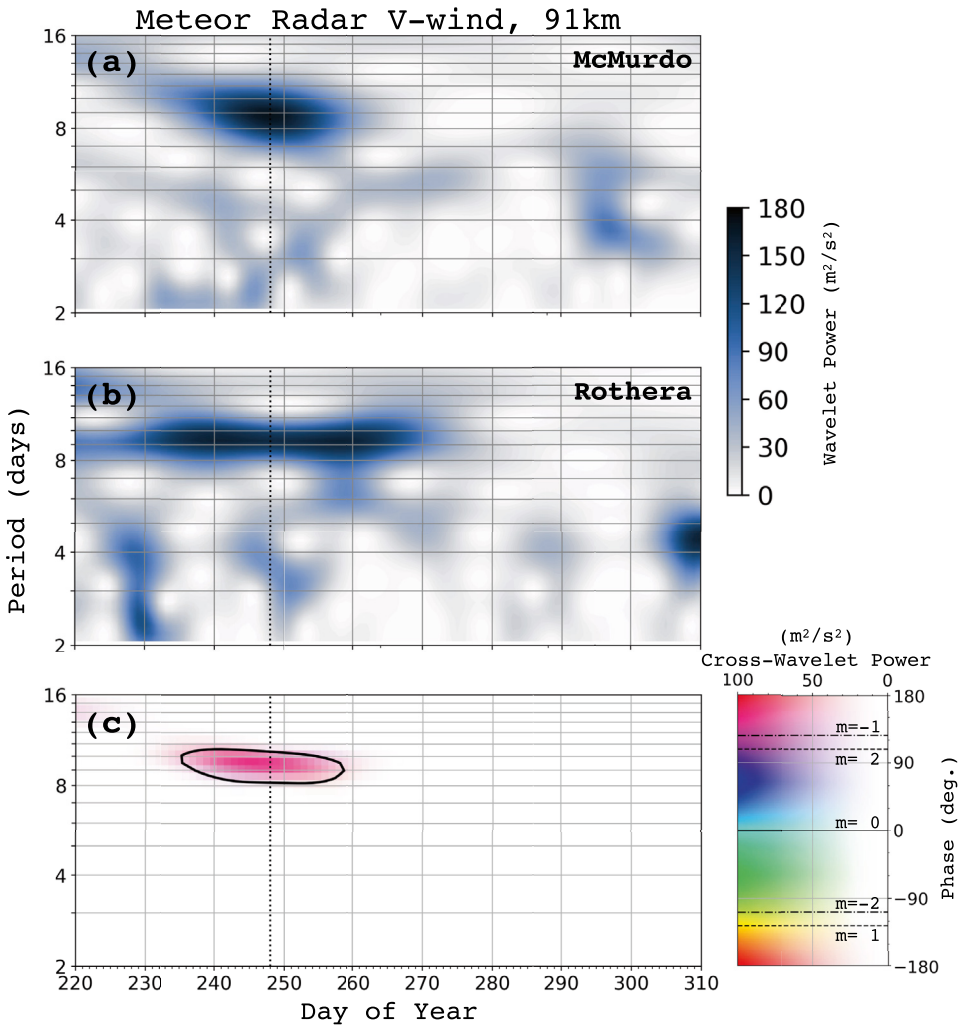

Figure 1. Wavelet spectra of the meridional wind at 91 km from (a) McMurdo station (77°51′S, 166°40′E), (b) Rothera station (67°34′S, 68°07′W) in Antarctica. (c) Cross-wavelet spectrum between McMurdo and Rothera stations. The color hue shows the phase difference between (a) and (b), where negative wave number (m) represents westward-propagating waves. Dashed vertical lines indicate the day of sudden stratospheric warming onset (2019 day 248). Black solid contour in Figure (c) shows the 99% confidence level.

(±45°) latitude, with a peak amplitude of ~200 m (~300 m). The prominent Q6DW in the middle atmosphere during the 2019 Southern SSW has been reported previously and is likely excited/amplified due to the barotropic/baroclinic instability during the SSW (Yamazaki et al., 2020). The Q6DW has also been recognized as an important agent in the coupling of the neutral atmosphere and ionosphere (Goncharenko et al., 2020; J. T. Lin et al., 2020; Miyoshi & Yamazaki, 2020). Given the strength of the Q6DW in Figure 2, and the latitude-height structures of Q6DW temperatures, geopotential heights and zonal and meridional winds in GCM simulations (e.g., Gan et al., 2016; Miyoshi & Yamazaki, 2020), it is surprising that the cross-wavelet analysis in Figure 1 does not reveal the Q6DW. We do not as yet have a viable explanation for this fact.

Figure 3 depicts the height versus latitude structure of Q10DW-W1 from MLS GPH and SABER temperature measurements for a fit window centered at day 260. For SABER temperature, there is clearly a bimodal structure in amplitude with one peak of ~5.5 K at 85 km and ±40–45° latitudes, and another peak of ~8K at 110 km. The observed amplitude is roughly 100% larger than the climatological amplitudes of the Q10DW-W1 from SABER measurements during the year 2002–2013 (Forbes & Zhang, 2015). It is also worth noting that the two peaks are roughly 180° out of phase (Figure 3c). This bimodal vertical structure

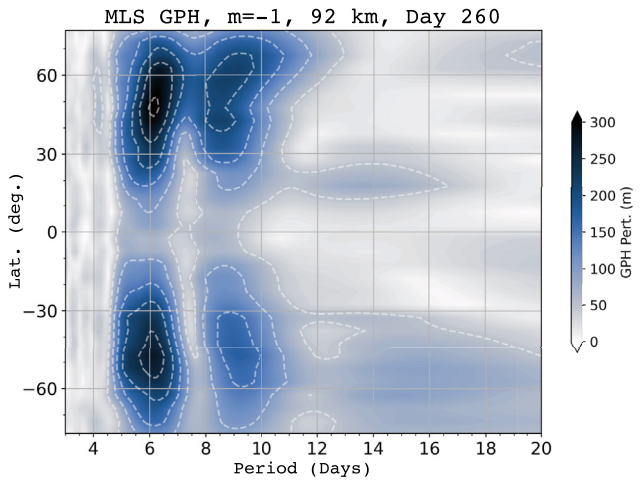

Figure 2. Latitude versus period of MLS geopotential height amplitudes, westward propagating zonal wave number one wave at an altitude of ~92 km for an analysis window centered on day 260. Contour level is 50 m.

in temperature amplitude likely results from the vertical gradient of GPH perturbation since the temperature ($T'(z)$) and GPH perturbation ($\Phi'(z)$) can be related by the hydrostatic equation

$$T'(z) = \frac{H}{R}\frac{\partial}{\partial z}\Phi'(z)$$

where R is the gas constant for dry air and H is the atmospheric scale height (Palo et al., 2007; Sassi et al., 2002). Accordingly, a single peak is expected to be found in the GPH perturbation near the altitude where the temperature perturbation reaches a minimum. This temperate perturbation minimum is expected to be out-of-phase above and below the peak of the GPH perturbation. This is evident in Figure 3b, where a single peak in GPH amplitude is located at ~92 km.

The MLS GPH has a distinct single peak at 60°S and ~35 km height with an amplitude of 250 m, suggesting an asymmetric amplitude structure in the stratosphere. Above this peak the GPH decreases to a minimum at 60 km and then begins to increase with increasing height. The amplitude of the MLS GPH becomes more symmetric above 60 km and has peaks near ±45° latitudes with amplitudes of 200 m in the Northern Hemisphere and 150 m in the Southern Hemisphere. Note that the observed amplitude is slightly smaller than the amplitudes of the Q10DW-W1 associated with the stratospheric final warmings in the Northern Hemisphere (Yamazaki & Matthias, 2019). Forbes and Zhang (2015) indicates that the Q10DW-W1 has a more intense response in the Northern Hemisphere than in the Southern Hemisphere due to the mean wind structure.

The phase structure of the Q10DW-W1 from SABER temperature observations shown in Figures 3c and 3d indicates that the dominant component is antisymmetric below 40 km height, but becomes symmetric above 40 km. Note that the phase for symmetric modes is expected to be the same in both hemispheres, and is shifted by 180° for antisymmetric modes. In the MLS geopotential height observations, the antisymmetric component dominates in the stratosphere and transitions toward a symmetric mode between 45 and 80 km (Figure 3f). The westward tilting phase structure with height (decreasing slope with altitude) indicates upward propagation of the Q10DW-W1 (Figure 3e). This result is contrary to the theoretical expectation for an unforced Rossby NM with a period of ~10 days, which is expected to be an antisymmetric (1,−3) NM (Forbes, 1995; Hough, 1898). This result suggests that the observed Q10DW in the MLT region is likely driven by a different mechanism other than the expected resonant NM response of the atmosphere.

Figure 4 shows results from the theoretical solution of Laplace's tidal equation with the assumption of an isothermal, windless, dissipationless atmosphere. Note that the eigenfunctions of the eigenvalue problem for the Laplace's tidal equation that describe the latitudinal structure are often called Hough functions (Hough, 1898). The Hough functions used in this study are computed by using the Chebyshev collocation method, and a compact MATLAB code for this numerical method can be found in Appendix B2 presented by Wang et al. (2016). The Rossby NMs are a resonant oscillation and can exist in the presence of the rotation of the Earth without external forcing (Andrews et al., 1987; Forbes, 1995). It is widely believed that baroclinic/barotropic instability in the middle atmosphere can trigger the growth of a NM, and this initial growth is followed by a global response of the atmospheric resonant mode (Lieberman, 2003; Liu et al., 2004; Norton & Thuburn, 1999; Plumb, 1983; Yamazaki & Matthias, 2019). In classical theory, the resonance of the atmosphere, or unforced NM, can be predicted by solving Laplace's tidal equation. Assuming the forcing in the vertical structure equation is zero and a constant scale height ($H = 7.5$ km) exists for the isothermal atmosphere ($T = 256$K), a single equivalent depth ($h_n = 10.5$ km) can be yielded for a series of oscillations with specific periods and wave numbers. This NM solution has a period of 8.2 days with wave number $m = -1$ for the antisymmetric (1,−3) mode, while for the first symmetric (1,−2) mode the period is 4.95 days with wave number $m = -1$. Both solutions are indicated as a vertical gray dashed line in Figures 4a and 4c, respectively. In practice, the true dynamics is more complex, the presence of dissipation and nonuniform background states can shift the latitudinal structure away from the theoretical solution.

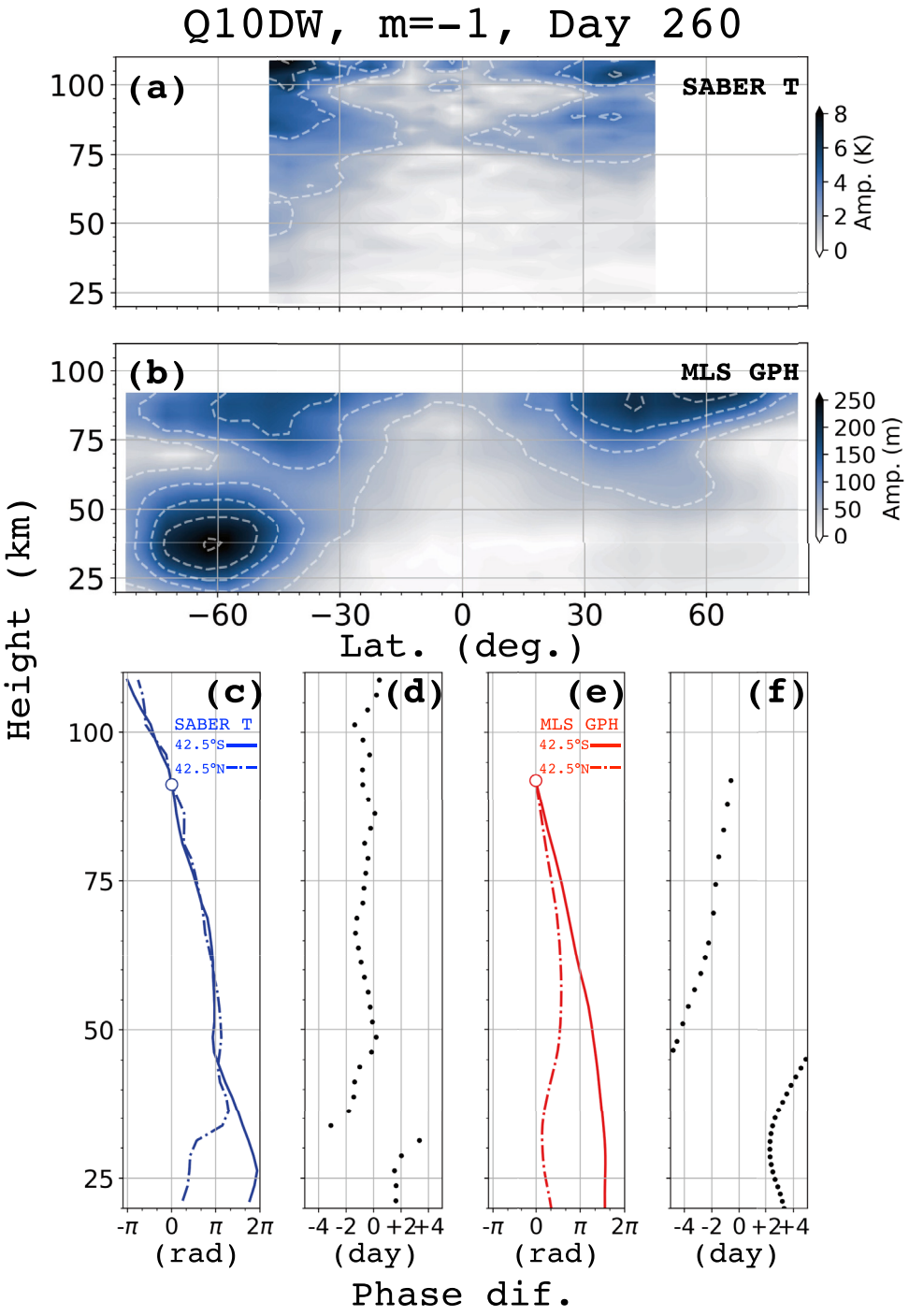

Figure 3. (a and b) Height versus latitude structure of the quasi-10 day planetary waves with zonal wave number one (Q10DW-W1) amplitude and (c and e) phase differences referenced to ~90 km height at (solid line) 42.5°S latitude (solid-dashed line) 42.5°N latitude for the analysis window centered on day 260. Open circle is the reference point for each vertical phase-difference profile. (d and f) Phase differences between 42.5°N and 42.5°S latitude. (a, c, and d) SABER temperature measurements. (b, e, and f) MLS geopotential height. Contour levels are 2 K and 50 m in Figures (a) and (b), respectively.

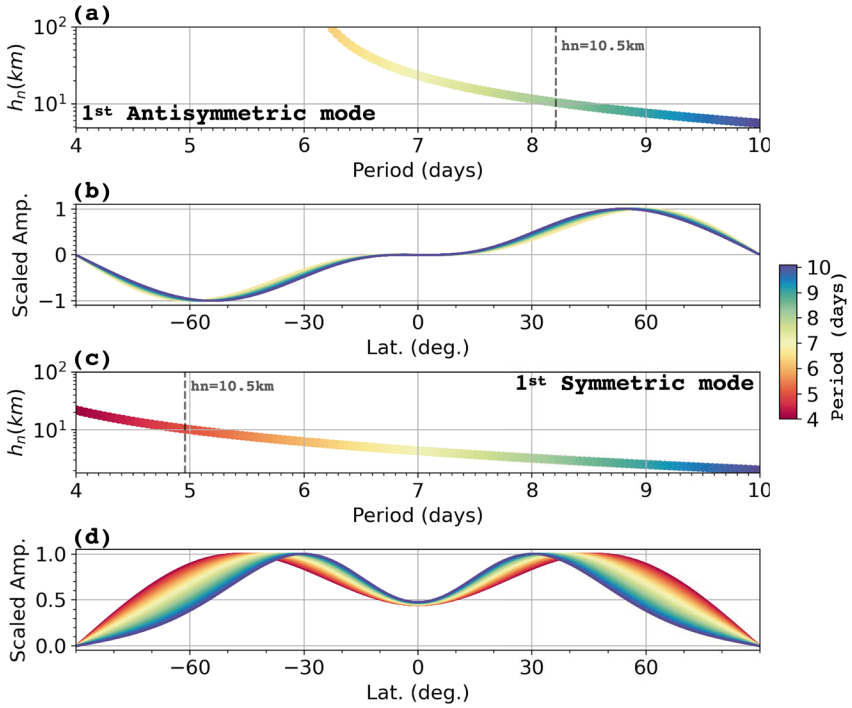

Figure 4. Hough function solutions for the westward propagating zonal wave number one wave from classical wave theory on a rotating sphere. Figures (a) and (c) show equivalent depth as a function of wave period. Figures (b) and (d) show latitudinal structure of normalized amplitudes for each solution. Figures (a) and (b) are for the first antisymmetric mode. Figures (c) and (d) are for the first symmetric mode. Gray vertical dashed lines in Figures (a) and (c) indicate where the equivalent depth is 10.5 km, which is the solution for the unforced normal mode in the isothermal, windless, dissipationless atmosphere.

Salby (1981) demonstrated numerically that the resonant response still occurs near the expected frequency and wave numbers of the theoretical solution although the response tends to be spread in frequency due to the Doppler shifting by the mean wind. Given that background, it is unlikely the symmetric Q10DW-W1 observed in 2019 Southern SSW is a NM since the equivalent depth for the symmetric Q10DW-W1 is too short to be amplified as a resonant oscillation mode in the middle atmosphere. The mean temperature required to result in such a NM translates to an equivalent depth of 2.5 km for the symmetric Q10DW-W1 is 61 K, which is ~100 K lower than the expected mean temperature in the middle atmosphere during the austral summer (Ramesh et al., 2020). This result suggests that there is more likely a forcing mechanism to excite the upward propagating symmetric Q10DW-W1 observed during the 2019 SSW.

To better illustrate the symmetric component of the Q10DW-W1, the wave perturbation is decomposed into its symmetric and antisymmetric parts about the equator. The symmetric and antisymmetric parts are defined as follows:

$$F(\phi) = FS(\phi) + FA(\phi)$$

where ϕ is latitude, and the function F consists of an antisymmetric part, FA, and a symmetric part, FS. Note, by definition:

$$\begin{aligned} FS(\phi) &= FS(-\phi) \\ FA(\phi) &= -FA(-\phi) \end{aligned}$$

and

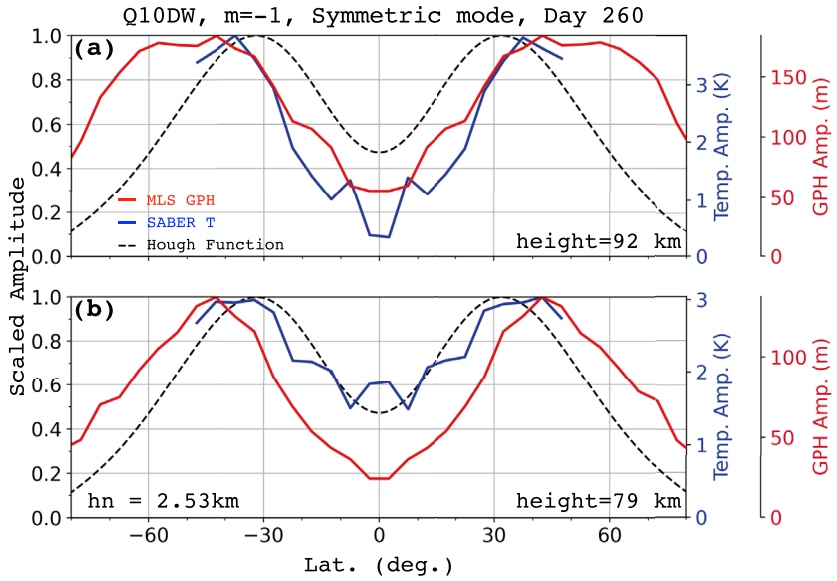

Figure 5. Latitudinal structure of the symmetric component of quasi-10 day planetary waves with zonal wave number one (Q10DW-W1) from (red) MLS geopotential height, (blue) SABER temperature, and (black dashed line) Hough function solution at an altitude of (a) 92 km and (b) 79 km for an analysis window centered on day 260.

$$FS(\phi) = [F(\phi) + F(-\phi)] / 2$$
$$FA(\phi) = [F(\phi) - F(-\phi)] / 2$$

Figure 5 shows the symmetric component of Q10DW-W1 from SABER temperature and MLS GPH at 79 and 92 km, as well as the corresponding latitudinal structure of the normalized Hough function solution for the (1,−2) mode at a period of 9 days. Note that this dominant periodicity is determined from the spectral analysis shown in the previous section.

The observed peaks in Figure 5 maximize between ±35° to ±45° latitudes, with an amplitude of ~135 meters (GPH) and 3 K (temperature) at a height of 79 km, and ~180 meters and ~4 K at 92 km. The latitudinal structure of temperature perturbations at 79 and 92 km are shifted poleward by ~10° relative to the theoretical solution. For the GPH the peak at 79 km, it is slightly poleward of that of the SABER temperature perturbation and a deeper minimum is seen at the equator. At a height of 92 km, the GPH latitude structure is considerably broader than the theoretical prediction, and extends into the high latitude regions. It is not uncommon to see the observed latitude structure deviate from the theoretical latitudinal structure, since mean winds can have the impact of moving tidal and/or planetary wave latitude structures poleward relative to the theoretical prediction (Gasperini et al., 2017; Ortland, 2005; Salby, 1981). Dissipation might also play a role in broadening the latitudinal structure when the wave propagates into the MLT region (Forbes & Vincent, 1989; Gasperini et al., 2017).

Figure 6 shows the vertical profile of the Q10DW-W1 phases difference and amplitudes in temperature and GPH at 42.5°S for an analysis window centered on day 260. Note that the phase difference is computed using a reference phase at 40 km. The westward phase tilt with height (decreasing phase with height) is apparent in both temperature and GPH perturbations, but a measureable phase difference is evident between the MLS GPH and SABER temperature differences. The difference is about $\frac{\pi}{2}$ (90°) at the height of 60 km, and this difference persists up to 90 km.

The vertical wavelength can be determined from the observed phase tilt and is calculated by the linear regression fit between a height of 65 and 92 km, shown as red solid and blue dashed lines in Figure 6a. The vertical wavelength is estimated to be 58.8 ± 1.9 km for SABER temperature, and 69.7 ± 1.7 km for MLS GPH. Note that the vertical wavelength in SABER temperature becomes noticeably shorter above 95 km.

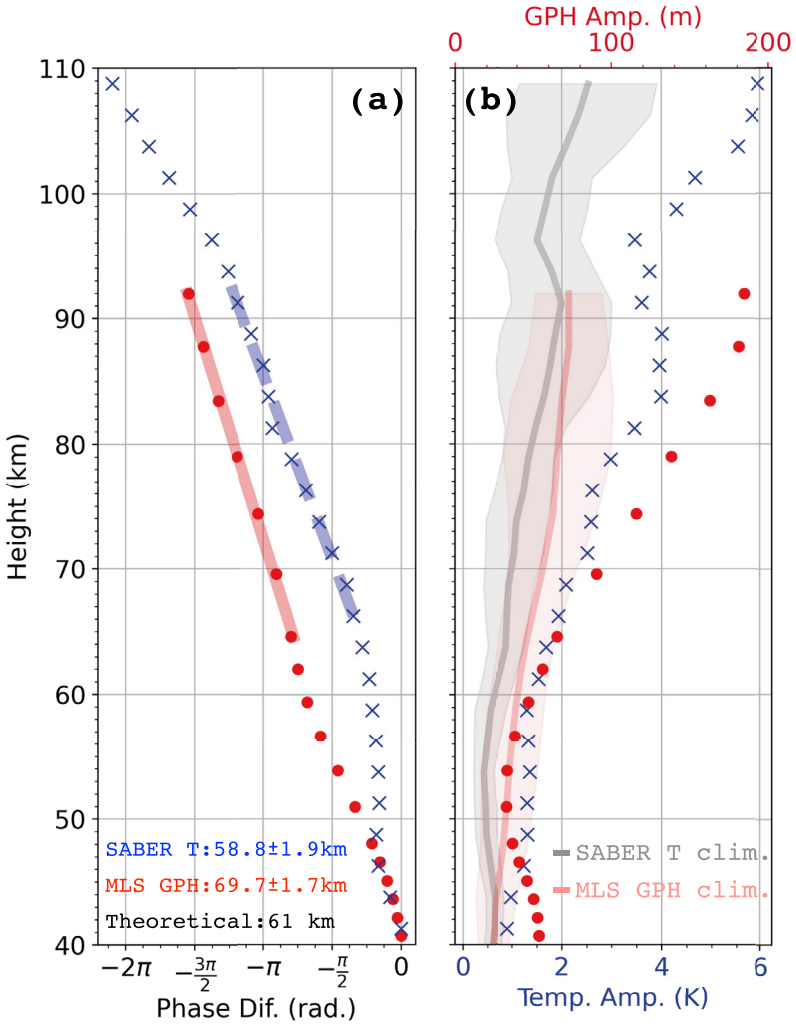

Figure 6. (a) Phase differences referenced to 40 km and (b) amplitude of the quasi-10 day planetary waves with zonal wave number one (Q10DW-W1) symmetric component at 42.5°S latitude for the analysis window centered on day 260. (blue) SABER temperature. (red) MLS geopotential height. Gray and pink lines in Figure (b) represent the mean amplitudes of the Q10DW-W1 symmetric component averaged over 2002–2018 for SABER temperature and MLS geopotential height, respectively, and shaded areas show the corresponding one standard deviation. The red solid and blue dashed lines in (a) are estimated of the vertical wavelength, which is 58.8 ± 1.9 km for SABER temperature, 69.7 ± 1.7 km for MLS geopotential height, and the theoretical Hough function solution is 61 km.

The theoretical vertical wavelength, λ_z, in an isothermal, windless, dissipationless atmosphere can be calculated from the equivalent depth, h_n, as follows (Forbes, 1995),

$$\lambda_z = \frac{2\pi H}{\sqrt{\frac{\kappa H}{h_n} - 0.25}}$$

where H is the scale height, and κ is $\frac{R}{C_p} \approx \frac{2}{7}$. For an isothermal atmosphere at 256 K (200 K), the vertical wavelength for the first symmetric mode with a period of 9 days is ~61 km (~58 km). This value is in excellent agreement with the estimated vertical wavelength for the temperature perturbation (58.8 ± 1.9 km) and is slightly smaller than the estimated vertical wavelength for the MLS GPH perturbation (69.7 ± 1.7 km). The consistency between the propagating analytical solution and observations provides strong evidence

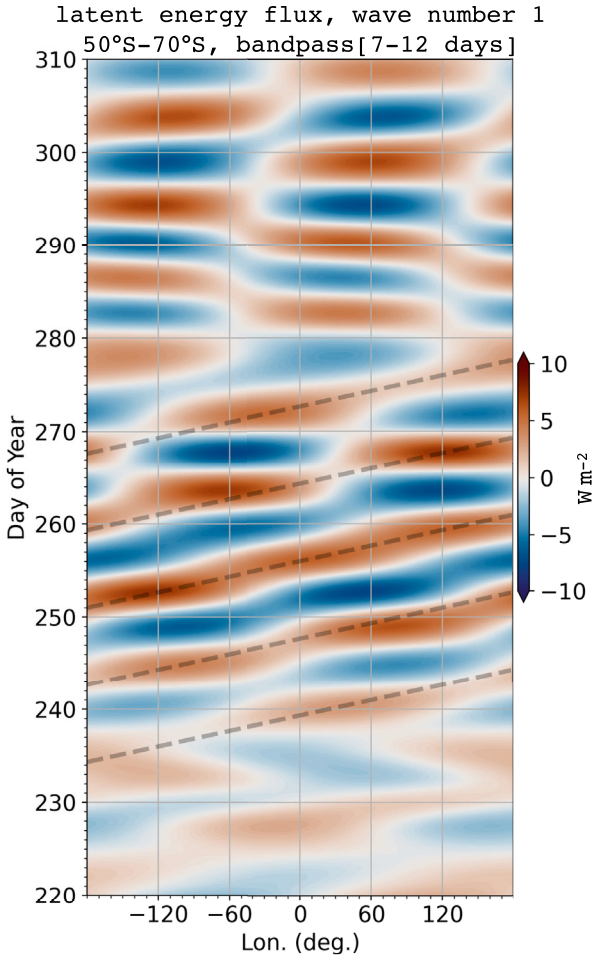

Figure 7. Bandpassed Hovmöller diagram for the wave number one component of the surface latent energy flux from MERRA-2 reanalysis averaged over 50°S–70°S. The stationary planetary wave number one component (SPW1) is removed. Gray dashed lines indicate the eastward quasi-10 day wave one (Q10DW-E1) consistent phase progression.

that this symmetric part of the Q10DW-W1 is consistent with theory and is likely excited from the lower atmosphere. It is possible that the evolution of SSW creates a unique dynamical and thermal structure which excites and/or amplifies this forced oscillation, and the resulting symmetric Q10DW-W1 then propagates vertically into the MLT region under these disturbed atmospheric conditions.

The Q10DW-W1 temperature amplitude in the Southern Hemisphere clearly shows a bimodal structure, as seen in Figure 3a, which is driven by the vertical gradient of the GPH perturbation as noted earlier. The peak can reach 4 K at 80–90 km, and 6 K at 110 km height. The GPH amplitude shows a peak at 92 km with an amplitude of ~190 m, and a local peak at 40 km with an amplitude of 60 m. Both temperature and GPH amplitudes are 100% or more larger than the climatological amplitudes, indicating that the symmetric Q10DW-W1 is not part of normal planetary wave activity in the middle atmosphere during the time period.

As noted earlier, the observed symmetric Q10DW-W1 is likely to be a forced mode, therefore an external forcing with a period around 10 days is required. The origin of the forcing of the Q10DW-W1, and the nature of its excitation mechanism are key questions to consider. It is reported that the occurrence of SSWs is well linked with tropospheric planetary wave forcing (Baldwin et al., 2020; Ding et al., 2011; Nishii et al., 2009). The wave number one eddy heat flux from the troposphere during the 2019 SSW is the strongest on record, and is attributed to a mid-latitude Rossby wave packet that is maintained by anomalous convective activities before the 2019 Southern SSW (Shen et al., 2020b). It is therefore reasonable to speculate that the Q10DW forcing originated from the troposphere. To test this hypothesis, the latent energy flux from the Modern-Era Retrospective analysis for Research and Applications, Version 2 (MERRA-2; Gelaro et al. (2017)) is examined to determine if wave forcing with a period near 10 days is present in the troposphere.

Figure 7 shows a longitude-time cross-section (Hovmöller diagram) of the wave number one component of surface latent energy flux averaged over 50°S-70°S latitudes which has been bandpassed. This Hovmöller diagram clearly illustrates amplification of the tropospheric forcing of the Q10DW-E1 (eastward propagating wave number one with a period near 10 days) during the 2019 SSW (days 240–270). Further, this wave-activity generation in the Southern Hemisphere tropospheric polar region is found to be capable of propagating into the stratosphere, as described below.

Figure 8 shows the vertical structure of Q10DW-E1, SPW1, and SPW2 GPH amplitudes for an analysis window centered on day 245. Investigating the spectra of planetary waves in the middle atmosphere during the SSW onset, the following planetary waves were detected: Q6DW-W1, Q10DW-E1, SPW1, SPW2, and Q10DW-W1. The SPW1 attains a maximum with amplitude of ~1,800 m at 65°S and 40 km height while the SPW2 peaks at 55°S and 40 km height with a amplitude of 400 m. The maximum Q10DW-E1 amplitude of 500 m occurs at 70°S and 45 km height.

It is well established that when the wave amplitudes become sufficiently large, second order nonlinear effects may play a significant role in the wave structure (Teitelbaum & Vial, 1991). This nonlinear interaction is manifested through advective terms in the momentum and thermodynamic equations, and results in two child waves with frequencies and wave numbers that are the sum and difference of the primary interacting PWs. A planetary wave perturbation can be written as follows, $A\cos(2\pi ft - m\lambda)$, where A is the wave amplitude, t = UT in days, λ = longitude, $f = \frac{1}{T}$, and T is the planetary wave period in days. The frequency and wave number of the sum wave is $f_s = f_1 + f_2$ and $m_s = m_1 + m_2$, and for the difference wave the

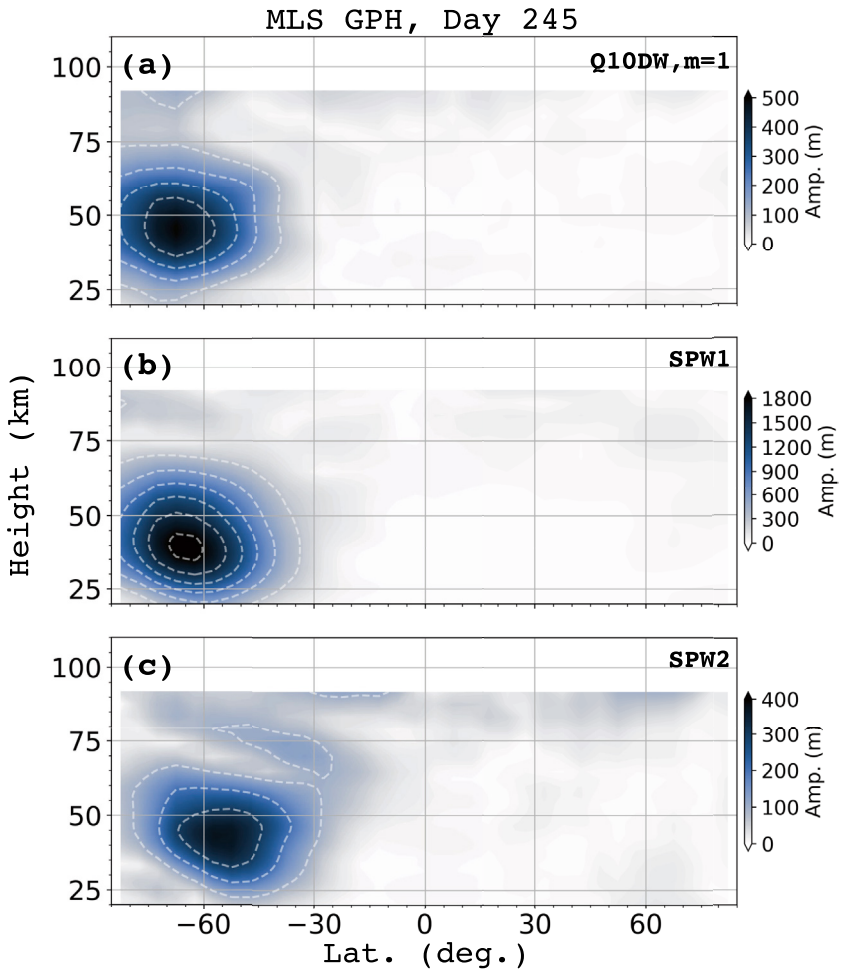

Figure 8. Height versus latitude structure of the (a) eastward quasi-10 day planetary wave number one (Q10DW-E1), (b) stationary planetary wave number one (SPW1), (c) SPW2 MLS geopotential height amplitudes for an analysis window centered on day 260. Contour level is 100 m in Figures (a) and (c), and 300 m in Figure (b).

frequency and wave number is $f_d = f_1 - f_2$ and $m_d = m_1 - m_2$. For example, a nonlinear interaction between the Q10DW-E1 and the SPW2 would produce child waves with periods of 10 days and westward propagating wave with zonal wave number one (Q10DW-W1), and eastward propagating wave with zonal wave number three (Q10DW-E3). The Q10DW-E1 interacting with SPW1 will produce child waves with wave numbers of zero (Q10DW-S0, Q10DW with zonal wave number zero) and two (Q10DW-E2, eastward propagating Q10DW with zonal wave number two).

The presence of Q10DW-E1 and SPW2 in the stratosphere clearly indicates these waves can propagate vertically into the middle atmosphere, and suggests that they can interact nonlinearly to excite the Q10DW-W1. Given the large amplitude of the SPW1 in the stratosphere, it is possible that the Q10DW-S0 and Q10DW-E2 are also excited in the middle atmosphere through a similar forcing mechanism.

Figures 9a and 9b show the vertical structure of Q10DW-S0 amplitudes for an analysis window centered on day 245. The vertical structure of Q10DW-E2 amplitudes for an analysis window centered on day 245 is provided in Figure S1 in the supporting material. The GPH amplitudes can reach ~350 m in the Southern Hemisphere polar region at 50 km height and the maximum in the Arctic appears slightly higher at 60 km altitude with an amplitude of ~250 m. The vertical bimodal structure in the Southern Hemisphere GPH amplitude is obvious, with nodes located at 75 km in the Antarctic and possibly 85 km in the Arctic although the MLS GPH data does not extend 90 km to validate this assertion. The temperature amplitude of the Q10DW-S0 can attain 6 K at 20°–30°S latitude and 110 km height although this occurs at the upper edge

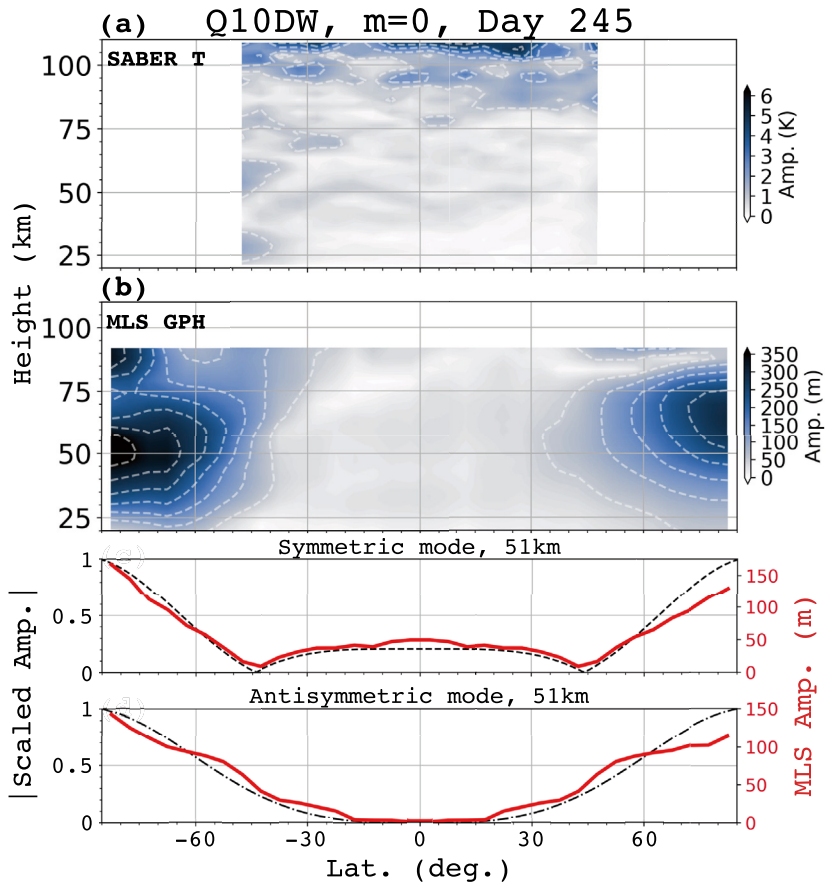

Figure 9. Height versus latitude structure of stationary the quasi-10 day planetary wave (Q10DW) (a) MLS geopotential height, (b) SABER temperature amplitudes for an analysis window centered on day 245. The corresponding latitudinal structure of the (c) symmetric mode, (d) antisymmetric component of the stationary Q10DW from MLS geopotential height (red line). Black dashed line is the absolute value of Hough function solution at an altitude of 51 km. Contour level is 1 K and 50 m in Figures (a) and (b), respectively.

of the SABER measurements where the uncertainty is largest. These results provide strong evidence that the Q10DW-S0 could be induced through a nonlinear interaction between the SPW1 and the Q10DW-E1, and additionally that the Q10DW-W1 is also likely generated through a nonlinear wave-wave interaction between the Q10DW-E1 and the SPW2.

Figures 9c and 9d show the symmetric and antisymmetric GPH components of the Q10DW-S0 at 51 km and the corresponding Hough function solutions for the first $m = 0$, 10 days symmetric and antisymmetric modes. Comparing the components of Q10DW-S0 with the theoretical Hough function solutions, it is shown that both modes are excited and the observed latitudinal structures of Q10DW-S0 are in a good agreement with the solutions of Laplace's tidal equation. These results demonstrate that the Q10DW-S0 is likely a forced mode and that the latitudinal structures in the middle atmosphere follow the analytical prediction. Closer to the MLT region, the latitudinal structure clearly deviates from the Hough function solution. The presence of dissipation and nonuniform background states could play a role and shift these solutions away from theory, which is not uncommon when waves propagate into the MLT region (Forbes & Zhang, 2015). It is also possible that the Q10DW-S0 in the MLT is the result of an oscillation of background mean state at the period of the traveling PWs (Pancheva et al., 2009). Such an oscillation could result from the fluctuation of the Eliassen-Palm flux divergence induced by wave-wave interactions (Forbes, Zhang, et al., 2018; Salby & Garcia, 1987) and wave-mean interactions (Smith, 1985). Especially during the SSW, the strong SPW1 is likely to interact nonlinearly with the traveling PWs and drive the background mean state at the periods of the PWs. Another possibility is that the Q10DW-S0 in the MLT is a secondary wave generated through a

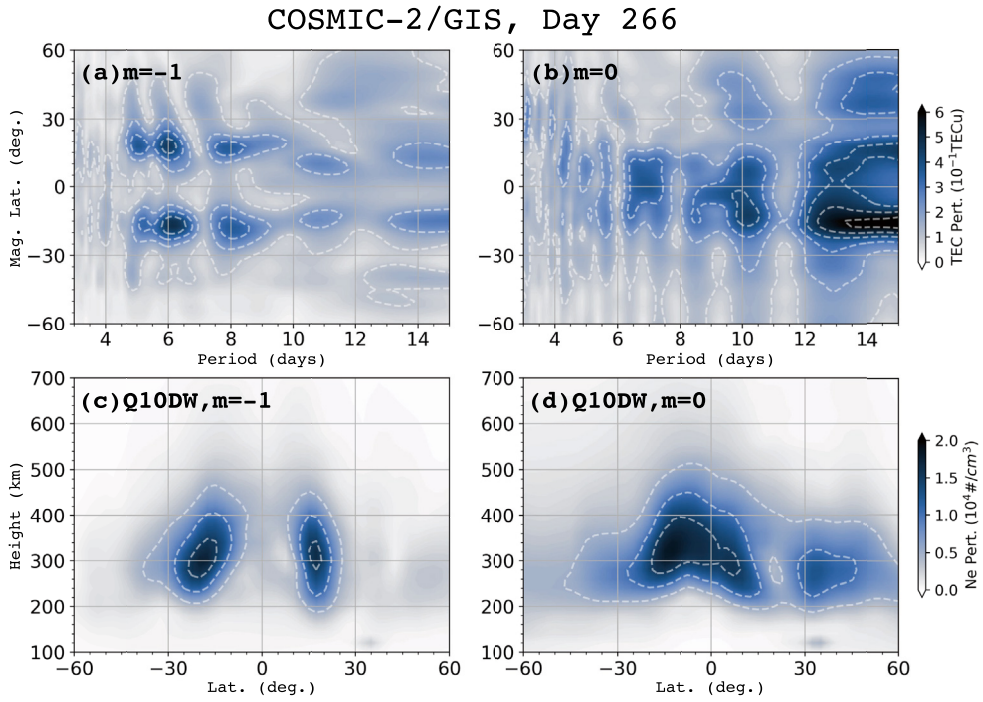

Figure 10. (a–b) Latitude versus period of COSMIC-2/global ionosphere specification total electron content (TEC) amplitudes for (a) the westward propagating zonal wave number one, (b) the zonally symmetric waves ($m = 0$) for an analysis window centered on day 266. Contour level is 0.1 TECu. (c–d) Vertical structure of the (c) westward propagating quasi-10-day oscillation with zonal number one (Q10DO-W1) and (d) zonally symmetric quasi-10-day oscillation (Q10DO-S0) amplitudes from COSMIC-2/global ionosphere specification electron density for an analysis window centered on day 266. Contour level is 0.5×10^4#/cm^3.

momentum deposition due to the gravity waves and/or tides filtered by the underlying planetary wave wind field in the stratosphere (Forbes & Zhang, 2015; Forbes et al., 2020; Lieberman et al., 2013; Smith, 1996). Such secondary generation of planetary waves might also play a role in the Q10DW-W1, but it is not apparent in the MLT region. Further investigation about the origin of these oscillations requires a numerical model and is beyond the scope of the present work.

3.2. Quasi 10-Day Oscillations in the Ionosphere

Having demonstrated that Q10DWs (W1, S0, E1) are present and amplified during the 2019 Southern SSW, it is possible to analyze the ionospheric response to determine if a coupling exists between the neutral atmosphere and ionosphere during the 2019 SSW. Figure 10 shows the COSMIC-2/GIS TEC periodogram of westward propagating waves with zonal wave number one and zero along with the corresponding vertical structure of PW oscillations in COSMIC-2/GIS electron density for an analysis window centered on day 266. Note that the $F_{10.7}$ solar radio flux and K_p index are generally less than 70 and 4 throughout much of the analysis window, indicating a low level of solar and geomagnetic activity. Three distinct peaks can be identified in Figure 10a: At 5.5 days, 6.5 days, and 8.5 days, concentrated near the crest region of the equatorial ionization anomaly (EIA).

For the zonal wave number zero oscillation (i.e., the zonally symmetric oscillations in Forbes, Zhang, et al. (2018)) the dominant periodicities are 6–7 days, 8.5 days, 10 days, and 13–14 days (Figure 10b). The 13.5-day periodicity in the zonally symmetric TEC oscillation is a common feature, and the wavelet analysis of K_p index also shows a significant 13.5-day periodicity during the analysis period (figure not shown). This periodic perturbation can be attributed to a similar periodicity in solar extreme ultraviolet radiation and geomagnetic activity (Lei et al., 2008; Mursula & Zieger, 1996). Other dominant periodicities (6–7 days, 8.5 days, and 10 days) in TEC are not present in the wavelet analysis of K_p index or $F_{10.7}$ solar radio flux,

indicating such periodicities are unlikely related to the solar forcing. It is also noteworthy that the latitudinal structure of TEC for the zonally symmetric oscillation ($m = 0$) has a different behavior compared with that of the $m = -1$ oscillation. The peaks for the zonally symmetric oscillation generally maximize near 10°S geomagnetic latitude with a secondary peak at the Northern low latitude region regardless of period, while the maxima for the $m = -1$ oscillation are located near ±15°–20° geomagnetic latitude, and the magnitudes between the austral and boreal peaks are roughly equal.

The vertical electron density structure for the quasi-10-day oscillations (Q10DOs) centered on day 266 are shown in Figures 10c and 10d, respectively. The Q10D0-W1 has two peaks maximizing at altitude near 300 km and ± 17.5° magnetic latitudes. This vertical and latitudinal distribution of electron density generally aligns with the crest of the EIA. This PW oscillation accounts for ±10%–15% of the variation in electron density and TEC about the mean. This value is reasonable and in the range of low-frequency ionospheric variability (periods of ∼2–30 days) which has been previously reported due to meteorological influences on the ionosphere from below during geomagnetically quiet times (Forbes et al., 2000). In contrast, the zonally symmetric oscillation in electron density has a distinct single peak in the Southern tropical region maximizing at 330 km height with a latitudinal extent spanning from 30°S to 10°N magnetic latitude. There is also a secondary peak located at 30°N-40°N magnetic latitudes, 280 km height.

The distinct difference in behavior between $m = 0$ and $m = -1$ TEC oscillations displayed in Figure 10 could indicate that the underlying mechanisms for these oscillations are different. The $m = -1$ ionosphere response appears to be the classic EIA response to electric fields generated in the dynamo region, perhaps modified by the presence of Q10DW-modulated tides (e.g., Forbes, Maute, et al., 2018) and/or secondary waves generated by such interactions (e.g., Gan et al., 2016; Miyoshi & Yamazaki, 2020; Nystrom et al., 2018). Conversely, the Q10DO-S0 oscillation in TEC contain a strong response equatorward of the EIA peak location. Therefore, although $m = 0$ oscillations in $E \times B$ drifts at PW periods exist in the simulations of Forbes, Maute, et al. (2018), an alternative mechanism is sought to explain the equatorial-region response of the Q10D0-S0. One possibility is a chemical effect. $[O]/[N_2]$ $m = 0$ variations at a 10-day period could occur if the vertically propagating tidal spectrum is modulated and dissipated with this periodicity (Gan et al., 2017; Jones et al., 2014; Yamazaki & Richmond, 2013), and/or the eddy diffusion near the turbopause is modulated by the Q10DWs filtering of the gravity waves from below (Nguyen & Palo, 2014). The latter mechanism has been demonstrated that it is more sensitive to longer-period planetary waves due to the non-negligible response time of the upper atmosphere. There are other factors that could also be at play such as wave-number coupling connected with zonal asymmetries in the magnetic field (Jones et al., 2013; Yue et al., 2013). A more definitive explanation of the Q10DW ionosphere response requires modeling directed toward identification of possible competing mechanisms.

Figure 11 shows the temporal variation of COSMIC-2/GIS TEC average amplitude of Q10DO-W1 and Q10DO-S0, along with the corresponding SABER amplitudes at 108.5 km. Note that the SABER amplitudes are shifted later in time by 6 and 9 days for Q10DW-W1 and Q10DW-S0, respectively, to account for vertical propagation time and to aid in the comparison. The 6- to 9-day time delay between the SABER temperature Q10DWs and the ionospheric PW activity could be attributed to the wave propagation time (Pedatella & Forbes, 2010) and the time needed for wave forcing to adjust and become steady (Vial et al., 1991), or time delays associated with producing chemical-based effects (Nguyen & Palo, 2014; Yamazaki & Richmond, 2013). The Q10DO-W1 in TEC increases from day 242 and peaks around day 266, and the Q10DO-S0, alternatively, has two peaks at day 257 and day 283. Both wave components in TEC gradually decrease after day 285. Similarly, the Q10DW perturbations show a similar temporal variation, suggesting a physical connection between the neutral temperature and perturbations observed in TEC. The correlation between the neutral atmospheric Q10DWs and the ionospheric Q10DOs is visually apparent. This coherence in temporal variation between the neutral and ionospheric features clearly demonstrates that the source of TEC perturbation near the period of 10 days originates in the neutral atmosphere and could be connected to the troposphere.

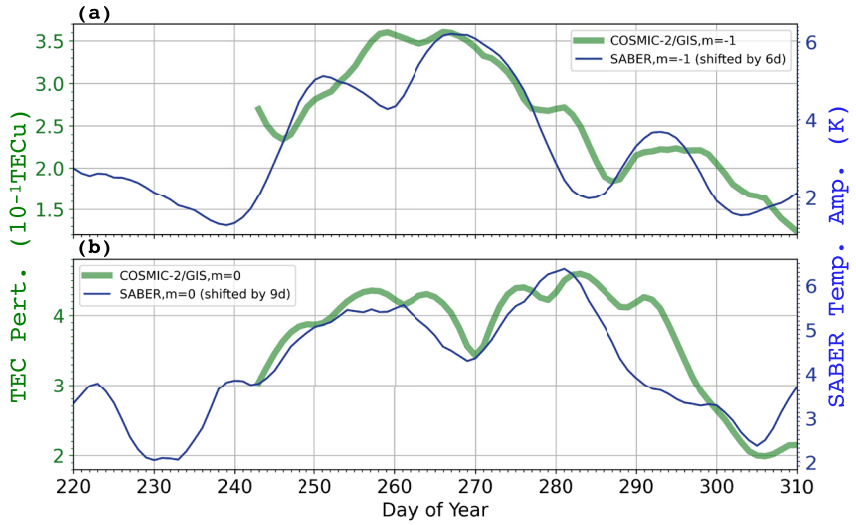

Figure 11. (a, green) westward propagating quasi-10-day oscillation with zonal number one (Q10DO-W1) amplitude versus day-of-year from COSMIC-2/global ionosphere specification (GIS) total electron content (TEC) averaged over 27.5°S to 17.5°S magnetic latitudes, and (a, blue) Q10DW-W1 SABER temperature amplitude averaged over 47.5°S to 32.5°S latitudes and 106.25 km, shifted by 6 days. (b, green) zonally symmetric quasi-10-day oscillation (Q10DO-S0) amplitude versus day-of-year from COSMIC-2/GIS TEC averaged over 22.5°S to 7.5°N magnetic latitudes, and (b,blue) Q10DW-S0 SABER temperature amplitude averaged over 17.5°N to 32.5°N latitudes and 106.25 km, shifted by 9 days.

4. Concluding Remarks

An unusual SSW occurred in the Southern Hemisphere in September 2019, which is one of only three Southern Hemisphere SSW (1988 minor SSW and 2002 major SSW) has been recorded (Shen et al., 2020a). The relatively low solar and geomagnetical levels during the onset of this SSW provide a fortuitous opportunity to investigate the coupling mechanisms between the neutral atmosphere and ionosphere through the amplification of planetary waves during the SSWs in the Southern Hemisphere. Ground-based and satellite observations show the clear presence of Q10DWs in both neutral atmosphere dynamics and ionospheric parameters during the SSW. The Q10DWs maximize in the MLT region approximately 10 days after the SSW onset. Analysis indicates that the Q10DW-W1 is a symmetric forced mode which is contrary to the classical theory for such planetary waves which predicts the Q10DW-W1 to be an antisymmetric NM. Forcing at a period near 10 days is likely driven by the amplification of Rossby wave activity in the troposphere. The results presented herein suggest that the Q10DW-W1 and Q10DW-S0 are potentially excited from a nonlinear wave-wave interaction between the Q10DW-E1 with SPW2 and SPW1, respectively. The Q10DW-W1 and Q10DW-S0 are also found to couple the ionosphere with the neutral atmosphere. Hourly electron density data from GIS was analyzed and prominent ionospheric Q10DOs were observed nearly concurrent with the neutral atmosphere wave activity. The timing of the Q10DOs in the ionosphere are consistent with those in the neutral atmosphere during a period of relatively low solar and geomagnetic activity, suggesting the Q10DWs play a key role in the ionospheric Q10DOs during the Southern SSW event. This study provides comprehensive observational evidence for coupling between the troposphere and ionosphere via the upward propagation of global scale planetary waves.

The results and conclusions presented herein can be summarized as follows:

- A symmetric forced Q10DW-W1 occurred during 2019 Southern Hemisphere SSW, contrary to theory which predicts the presence of an antisymmetric NM. The source of the Q10DW-W1 in the middle atmosphere likely results from the nonlinear wave-wave interaction between the Q10DW-E1 and SPW2. Examination of the surface heat flux data indicates that the forcing for the 10-day periodicity is driven by the eastward-propagating latent heat release at the period near 10 days in the troposphere.
- The vertical wavelength and latitudinal structure of the antisymmetric Q10DW-W1 is consistent with the corresponding Hough function solution for the forced (1,−2) mode. This result demonstrates that even

for the forced mode the response is still consistent with Laplace's tidal equation and Hough mode theory. Similar to prior results presented in Salby (1981) and Forbes and Zhang (2015), the latitudinal structure of the Q10DW-W1 tends to be broadened due to the presence of the mean wind and/or molecular dissipation in the MLT region.

- The manifestation of the Q10DW-S0 in the stratosphere supports the proposed excitation source of the Q10DW-W1. The reason for the deviation of the Q10DW-S0 latitudinal structure in the MLT cannot be conclusively determined. Further investigation regarding its origin is beyond the scope of the present work and will be addressed in future modeling studies.
- The coherence of temporal variation between atmospheric Q10DWs and ionospheric Q10DOs suggests a physical connection between the neutral atmosphere and ionosphere.

This study clearly demonstrates that the planetary waves are key drivers for coupling the neutral atmosphere and ionosphere during the SSW events. Our analysis indicates the Q10DWs play an important role in ionospheric variability during the Southern Hemisphere SSW events, and indicates that the Q10DWs can effectively couple the troposphere to the ionosphere.

Data Availability Statement

SABER data is available on GATS, Inc. web-platform (http://saber.gats-inc.com). MLS and MERRA-2 data were downloaded from the NASA's Earth Science Data Systems (https://doi.org/10.5067/Aura/MLS/DATA2021). GIS data is available on the National Cheng Kung University web-platform (http://formosat7.earth.ncku.edu.tw/). Data for the Rothera radar can be found at http://psddb.nerc-bas.ac.uk/data/access/coverage.php?menu=4&source=1&class=58&script=1. Meridional wind data for the McMurdo radar can be found at https://doi.org/10.5281/zenodo.4726135. We are grateful to the SABER, MLS, MERRA-2, GIS, and Rothera radar teams for open access to their respective data sets. The scientific color maps (https://doi.org/10.5281/zenodo.4153113; Crameri et al., 2020) are used in figures herein to prevent visual distortion of the data and exclusion of readers with color-vision deficiencies.

Acknowledgments
This research was supported by NSF grant AGS-1552286, part of the CEDAR program under the direction of Dr. Scott Palo. The meteor radar located at McMurdo Station was supported by NSF grant OPP-1543446. J.M. Forbes was supported under Award AGS-1630177 from the NSF Aeronomy Program. T. Moffat-Griffin and N.J. Mitchell are supported by the UK Natural Environment Research Council (grant nos. NE/R001391/1 and NE/R001235/1). This work was performed while J.C. Wang held a Government Scholarship for Study Abroad awarded by the Ministry of Education, Taiwan. J.C. Wang thanks to the high-performance computing support on Cheyenne (ark:/85065/d7wd3xhc) provided by NCAR's Computational and Information Systems Laboratory. J.C. Wang also acknowledges Dr. Han-Li Liu for his valuable discussions and comments. The National Center for Atmospheric Research is a major facility sponsored by the National Science Foundation under Cooperative Agreement No. 1852977.

References

Allen, D. R., Bevilacqua, R. M., Nedoluha, G. E., Randall, C. E., & Manney, G. L. (2003). Unusual stratospheric transport and mixing during the 2002 Antarctic winter. *Geophysical Research Letters*, *30*(12), 1–4. https://doi.org/10.1029/2003GL017117

Andrews, D. G., Leovy, C. B., & Holton, J. R. (1987). *Middle atmosphere dynamics*. Academic press.

Baldwin, M. P., Ayarzagüena, B., Birner, T., Butchart, N., Butler, A. H., Charlton-Perez, A. J., et al. (2020). Sudden stratospheric warmings. *Reviews of Geophysics*, *59*, e2020RG000708. https://doi.org/10.1029/2020rg000708

Butler, A. H., Seidel, D. J., Hardiman, S. C., Butchart, N., Birner, T., & Match, A. (2015). Defining sudden stratospheric warmings. *Bulletin of the American Meteorological Society*, *96*(11), 1913–1928. https://doi.org/10.1175/BAMS-D-13-00173.1

Butler, A. H., Sjoberg, J. P., Seidel, D. J., & Rosenlof, K. H. (2017). A sudden stratospheric warming compendium. *Earth System Science Data*, *9*(1), 63–76. https://doi.org/10.5194/essd-9-63-2017

Chandran, A., Collins, R. L., & Harvey, V. L. (2014). Stratosphere-mesosphere coupling during stratospheric sudden warming events. *Advances in Space Research*, *53*(9), 1265–1289. https://doi.org/10.1016/j.asr.2014.02.005

Chang, L. C., Liu, J. Y., & Palo, S. E. (2011). Propagating planetary wave coupling in SABER MLT temperatures and GPS TEC during the 2005/2006 austral summer. *Journal of Geophysical Research*, *116*(10), A10324. https://doi.org/10.1029/2011JA016687

Crameri, F., Shephard, G. E., & Heron, P. J. (2020). The misuse of colour in science communication. *Nature Communications*, *11*(1), 1–10. https://doi.org/10.1038/s41467-020-19160-7

Dawkins, E. C. M., Feofilov, A., Rezac, L., Kutepov, A. A., Janches, D., Höffner, J., et al. (2018). Validation of SABER v2.0 operational temperature data with ground-based lidars in the mesosphere-lower thermosphere region (75–105 km). *Journal of Geophysical Research: Atmospheres*, *123*(17), 9916–9934. https://doi.org/10.1029/2018JD028742

Ding, Q., Steig, E. J., Battisti, D. S., & Küttel, M. (2011). Winter warming in West Antarctica caused by central tropical Pacific warming. *Nature GSABERcience*, *4*(6), 398–403. https://doi.org/10.1038/ngeo1129

Elford, W. G., & Robertson, D. S. (1953). Measurements of winds in the upper atmosphere by means of drifting meteor trails II. *Journal of Atmospheric and Terrestrial Physics*, *4*(4–5), 271–284. https://doi.org/10.1016/0021-9169(53)90060-9

Eswaraiah, S., Kim, J., Lee, W., Hwang, J., Kumar, K. N., & Kim, Y. H. (2020). Unusual changes in the Antarctic middle atmosphere during the 2019 warming in the Southern Hemisphere. *Geophysical Research Letters*, *47*(19), 1–11. https://doi.org/10.1029/2020GL089199

Finlay, C. C., Maus, S., Beggan, C. D., Bondar, T. N., Chambodut, A., Chernova, T. A., et al. (2010). International Geomagnetic Reference Field: The eleventh generation. *Geophysical Journal International*, *183*(3), 1216–1230. https://doi.org/10.1111/j.1365-246X.2010.04804.x

Forbes, J. M. (1995). Tidal and planetary waves. In *Up. mesos. low. thermo sph. a rev. exp. theory* (pp. 67–87). American Geophysical Union (AGU). https://doi.org/10.1029/GM087p0067

Forbes, J. M., Maute, A., Zhang, X., & Hagan, M. E. (2018). Oscillation of the Ionosphere at planetary-wave periods. *Journal of Geophysical Research: Space Physics*, *123*(9), 7634–7649. https://doi.org/10.1029/2018JA025720

Forbes, J. M., Palo, S. E., & Zhang, X. (2000). Variability of the ionosphere. *Journal of Atmospheric and Solar-Terrestrial Physics*, *62*(8), 685–693. https://doi.org/10.1016/S1364-6826(00)00029-8

Forbes, J. M., & Vincent, R. A. (1989). Effects of mean winds and dissipation on the diurnal propagating tide: An analytic approach. *Planetary and Space Science*, *37*(2), 197–209. https://doi.org/10.1016/0032-0633(89)90007-X

Forbes, J. M., & Zhang, X. (2015). Quasi-10-day wave in the atmosphere. *Journal of Geophysical Research*, *120*(21), 11079–11111. https://doi.org/10.1002/2015JD023327

Forbes, J. M., Zhang, X., & Maute, A. (2020). Planetary Wave (PW) generation in the thermosphere driven by the PW-modulated tidal spectrum. *Journal of Geophysical Research: Space Physics*, *125*(5), 1–19. https://doi.org/10.1029/2019JA027704

Forbes, J. M., Zhang, X., Maute, A., & Hagan, M. E. (2018). Zonally symmetric oscillations of the thermosphere at planetary wave periods. *Journal of Geophysical Research: Space Physics*, *123*(5), 4110–4128. https://doi.org/10.1002/2018JA025258

Gan, Q., Eastes, R. W., Burns, A. G., Wang, W., Qian, L., Solomon, S. C., et al. (2020). New observations of large-scale waves coupling with the ionosphere made by the GOLD Mission: Quasi-16-day wave signatures in the F-region OI 135.6-nm nightglow during sudden stratospheric warmings. *Journal of Geophysical Research: Space Physics*, *125*(4), 1–9. https://doi.org/10.1029/2020JA027880

Gan, Q., Oberheide, J., Yue, J., & Wang, W. (2017). Short-term variability in the ionosphere due to the nonlinear interaction between the 6-day wave and migrating tides. *Journal of Geophysical Research: Space Physics*, *122*(8), 8831–8846. https://doi.org/10.1002/2017JA023947

Gan, Q., Wang, W., Yue, J., Liu, H., Chang, L. C., Zhang, S., et al. (2016). Numerical simulation of the 6-day wave effects on the ionosphere: Dynamo modulation. *Journal of Geophysical Research: Space Physics*, *121*(10), 10103–10116. https://doi.org/10.1002/2016JA022907

Gasperini, F., Forbes, J. M., & Hagan, M. E. (2017). Wave coupling from the lower to the middle thermosphere: Effects of mean winds and dissipation. *Journal of Geophysical Research: Space Physics*, *122*(7), 7781–7797. https://doi.org/10.1002/2017JA024317

Gelaro, R., McCarty, W., Suárez, M. J., Todling, R., Molod, A., Takacs, L., et al. (2017). The Modern-Era Retrospective Analysis for Research and Applications, Version 2 (MERRA-2). *Journal of Climate*, *30*(14), 5419–5454. https://doi.org/10.1175/JCLI-D-16-0758.1

Goncharenko, L. P., Chau, J. L., Liu, H. L., & Coster, A. J. (2010). Unexpected connections between the stratosphere and ionosphere. *Geophysical Research Letters*, *37*(10), L10101. https://doi.org/10.1029/2010GL043125

Goncharenko, L. P., Harvey, V. L., Greer, K. R., Zhang, S. R., & Coster, A. J. (2020). Longitudinally dependent low-latitude ionospheric disturbances linked to the antarctic sudden stratospheric warming of September 2019. *Journal of Geophysical Research: Space Physics*, *125*(8), 1–13. https://doi.org/10.1029/2020JA028199

He, M., Chau, J. L., Forbes, J. M., Thorsen, D., Li, G., Siddiqui, T. A., et al. (2020). Quasi-10-day wave and semidiurnal tide nonlinear interactions during the Southern Hemispheric SSW 2019 observed in the Northern Hemispheric mesosphere. *Geophysical Research Letters*, *47*(23), 1–9. https://doi.org/10.1029/2020GL091453

He, M., Chau, J. L., Stober, G., Li, G., Ning, B., & Hoffmann, P. (2018). Relations between semidiurnal tidal variants through diagnosing the zonal wavenumber using a phase differencing technique based on two ground-based detectors. *Journal of Geophysical Research: Atmospheres*, *123*(8), 4015–4026. https://doi.org/10.1002/2018JD028400

Hocking, W., Fuller, B., & Vandepeer, B. (2001). Real-time determination of meteor-related parameters utilizing modern digital technology. *Journal of Atmospheric and Solar-Terrestrial Physics*, *63*(2–3), 155–169. https://doi.org/10.1016/S1364-6826(00)00138-3

Hough, S. S. (1898). On the application of harmonic analysis to the dynamical theory of the tides. Part II. On the general integration of Laplace's dynamical equations. *Proceedings of the Royal Society of London*, *62*(379–387), 209–210. https://doi.org/10.1098/rspl.1897.0099

Jones, M., Forbes, J. M., & Hagan, M. E. (2014). Tidal-induced net transport effects on the oxygen distribution in the thermosphere. *Geophysical Research Letters*, *41*(14), 5272–5279. https://doi.org/10.1002/2014GL060698

Jones, M., Forbes, J. M., Hagan, M. E., & Maute, A. (2013). Non-migrating tides in the ionosphere-thermosphere: In situ versus tropospheric sources. *Journal of Geophysical Research: Space Physics*, *118*(5), 2438–2451. https://doi.org/10.1002/jgra.50257

Krüger, K., Naujokat, B., & Labitzke, K. (2005). The unusual midwinter warming in the Southern Hemisphere stratosphere 2002: A comparison to Northern Hemisphere phenomena. *Journal of the Atmospheric Sciences*, *62*(3), 603–613. https://doi.org/10.1175/JAS-3316.1

Labitzke, K. (1981). Stratospheric-mesospheric midwinter disturbances: A summary of observed characteristics. *Journal of Geophysical Research*, *86*(C10), 9665. https://doi.org/10.1029/JC086iC10p09665

Lei, J., Thayer, J. P., Forbes, J. M., Wu, Q., She, C., Wan, W., & Wang, W. (2008). Ionosphere response to solar wind high-speed streams. *Geophysical Research Letters*, *35*(19). https://doi.org/10.1029/2008GL035208

Lewis, D. (2019). Rare warming over Antarctica reveals power of stratospheric models. *Nature*, *574*(7777), 160–161. https://doi.org/10.1038/d41586-019-02985-8

Lieberman, R. S. (2003). The 6.5-day wave in the mesosphere and lower thermosphere: Evidence for baroclinic/barotropic instability. *Journal of Geophysical Research*, *108*(D20), 4640. https://doi.org/10.1029/2002JD003349

Lieberman, R. S., Riggin, D. M., & Siskind, D. E. (2013). Stationary waves in the wintertime mesosphere: Evidence for gravity wave filtering by stratospheric planetary waves. *Journal of Geophysical Research: Atmospheres*, *118*(8), 3139–3149. https://doi.org/10.1002/jgrd.50319

Lim, E.-P., Hendon, H. H., Butler, A. H., Garreaud, R. D., Polichtchouk, I., Shepherd, T. G., & Newman, P. A. (2020). *The 2019 Antarctic sudden stratospheric warming*. Retrieved from https://www.sparc-climate.org/wp-content/uploads/sites/5/2017/12/SPARCnewsletter%7B/%7DJan2020%7B/%7DWEB.pdf%7B/#}page=10

Limpasuvan, V., Orsolini, Y. J., Chandran, A., Garcia, R. R., & Smith, A. K. (2016). On the composite response of the MLT to major sudden stratospheric warming events with elevated stratopause. *Journal of Geophysical Research: Atmospheres*, *121*(9), 4518–4537. https://doi.org/10.1002/2015JD024401

Lin, C. Y., Lin, C. C., Liu, J., Rajesh, P. K., Matsuo, T., Chou, M., et al. (2020). The Early Results and Validation of FORMOSAT-7/COSMIC-2 Space Weather Products: Global Ionospheric Specification and Ne-Aided Abel Electron Density Profile. *Journal of Geophysical Research: Space Physics*, *125*(10), 1–12. https://doi.org/10.1029/2020JA028028

Lin, C. Y., Matsuo, T., Liu, J. Y., Lin, C. H., Huba, J. D., Tsai, H. F., & Chen, C. Y. (2017). Data assimilation of ground-based GPS and radio occultation total electron content for global ionospheric specification. *Journal of Geophysical Research: Space Physics*, *122*(10), 10876–10886. https://doi.org/10.1002/2017JA024185

Lin, C. Y., Matsuo, T., Liu, J. Y., Lin, C. H., Tsai, H. F., & Araujo-Pradere, E. A. (2015). Ionospheric assimilation of radio occultation and ground-based GPS data using non-stationary background model error covariance. *Atmospheric Measurement Techniques*, *8*(1), 171–182. https://doi.org/10.5194/amt-8-171-2015

Lin, J. T., Lin, C. H., Rajesh, P. K., Yue, J., Lin, C. Y., & Matsuo, T. (2020). Local-time and vertical characteristics of quasi-6-day oscillation in the ionosphere during the 2019 Antarctic Sudden stratospheric warming. *Geophysical Research Letters*, *47*(21). https://doi.org/10.1029/2020GL090345

Liu, H. L., & Roble, R. G. (2005). Dynamical coupling of the stratosphere and mesosphere in the 2002 Southern Hemisphere major stratospheric sudden warming. *Geophysical Research Letters*, *32*(13), 1–4. https://doi.org/10.1029/2005GL022939

Liu, H. L., Talaat, E. R., Roble, R. G., Lieberman, R. S., Riggin, D. M., & Yee, J. H. (2004). The 6.5-day wave and its seasonal variability in the middle and upper atmosphere. *Journal of Geophysical Research*, *109*(21), D21112. https://doi.org/10.1029/2004JD004795

Livesey, N. J., Read, W. G., Wagner, P. A., Froidevaux, L., Lambert, A., Manney, G. L., et al. (2017). *Version 4.2x Level 2 data quality and description document*, JPL D-33509 Rev. C (Tech. Rep.). Retrieved from http://mls.jpl.nasa.gov/data/v4-2_data_quality_document.pdf

Loon, van H., Jenne, R. L., & Labitzke, K. (1973). Zonal harmonic standing waves. *Journal of Geophysical Research*, *78*(21), 4463–4471. https://doi.org/10.1029/JC078i021p04463

Matsuno, T. (1971). A dynamical model of the stratospheric sudden warming. *Journal of the Atmospheric Sciences*, *28*(8), 1479–1494. https://doi.org/10.1175/1520-0469(1971)028<1479:ADMOTS>2.0.CO;2

Miyoshi, Y., & Yamazaki, Y. (2020). Excitation Mechanism of ionospheric 6-day oscillation during the 2019 September sudden stratospheric warming event. *Journal of Geophysical Research: Space Physics*, *125*(9). https://doi.org/10.1029/2020JA028283

Mo, X., & Zhang, D. (2020). Quasi-10 d wave modulation of an equatorial ionization anomaly during the Southern Hemisphere stratospheric warming of 2002. *Annales Geophysicae*, *38*(1), 9–16. https://doi.org/10.5194/angeo-38-9-2020

Mursula, K., & Zieger, B. (1996). The 13.5-day periodicity in the Sun, solar wind, and geomagnetic activity: The last three solar cycles. *Journal of Geophysical Research*, *101*(A12), 27077–27090. https://doi.org/10.1029/96JA02470

Nguyen, V., & Palo, S. E. (2014). Transmission of planetary wave effects to the upper atmosphere through eddy diffusion modulation. *Journal of Atmospheric and Solar-Terrestrial Physics*, *117*, 1–6. https://doi.org/10.1016/j.jastp.2014.04.008

Nishii, K., Nakamura, H., & Miyasaka, T. (2009). Modulations in the planetary wave field induced by upward-propagating Rossby wave packets prior to stratospheric sudden warming events: A case-study. *Quarterly Journal of the Royal Meteorological Society*, *135*(638), 39–52. https://doi.org/10.1002/qj.359

Norton, W. A., & Thuburn, J. (1999). Sensitivity of mesospheric mean flow, planetary waves, and tides to strength of gravity wave drag. *Journal of Geophysical Research*, *104*(D24), 30897–30911. https://doi.org/10.1029/1999JD900961

Nystrom, V., Gasperini, F., Forbes, J. M., & Hagan, M. E. (2018). Exploring wave-wave interactions in a general circulation model. *Journal of Geophysical Research: Space Physics*, *123*(1), 827–847. https://doi.org/10.1002/2017JA024984

Ortland, D. A. (2005). A study of the global structure of the migrating diurnal tide using generalized Hough modes. *Journal of the Atmospheric Sciences*, *62*(8), 2684–2702. https://doi.org/10.1175/JAS3501.1

Palo, S. E., Forbes, J. M., Zhang, X., Russell, I. M., Mertens, C. J., Mlynczak, M. G., et al. (2005). Planetary wave coupling from the stratosphere to the thermosphere during the 2002 Southern Hemisphere pre-stratwarm period. *Geophysical Research Letters*, *32*(23), 1–5. https://doi.org/10.1029/2005GL024298

Palo, S. E., Forbes, J. M., Zhang, X., Russell, I. M., & Mlynczak, M. G. (2007). An eastward propagating two-day wave: Evidence for nonlinear planetary wave and tidal coupling in the mesosphere and lower thermosphere. *Geophysical Research Letters*, *34*(7), 2–5. https://doi.org/10.1029/2006GL027728

Pancheva, D., Mukhtarov, P., Andonov, B., Mitchell, N. J., & Forbes, J. M. (2009). Planetary waves observed by TIMED/SABER in coupling the stratosphere-mesosphere-lower thermosphere during the winter of 2003/2004: Part 1-Comparison with the UKMO temperature results. *Journal of Atmospheric and Solar-Terrestrial Physics*, *71*(1), 61–74. https://doi.org/10.1016/j.jastp.2008.09.016

Pancheva, D., Mukhtarov, P., Mitchell, N. J., Andonov, B., Merzlyakov, E., Singer, W., et al. (2008). Latitudinal wave coupling of the stratosphere and mesosphere during the major stratospheric warming in 2003/2004. *Annales Geophysicae*, *26*(3), 467–483. https://doi.org/10.5194/angeo-26-467-2008

Pedatella, N. M., & Forbes, J. M. (2010). Evidence for stratosphere sudden warming-ionosphere coupling due to vertically propagating tides. *Geophysical Research Letters*, *37*(11), L11104. https://doi.org/10.1029/2010GL043560

Pedatella, N. M., & Liu, H. L. (2013). The influence of atmospheric tide and planetary wave variability during sudden stratosphere warmings on the low latitude ionosphere. *Journal of Geophysical Research: Space Physics*, *118*(8), 5333–5347. https://doi.org/10.1002/jgra.50492

Plumb, R. A. (1983). Baroclinic instability of the summer mesosphere: A mechanism for the quasi-two-day wave? *Journal of the Atmospheric Sciences*, *40*(1), 262–270. https://doi.org/10.1175/1520-0469(1983)040<0262:BIOTSM>2.0.CO;2

Ramesh, K., Smith, A. K., Garcia, R. R., Marsh, D. R., Sridharan, S., & Kishore Kumar, K. (2020). Long-term variability and tendencies in middle atmosphere temperature and zonal wind from WACCM6 simulations during 1850-2014. *Journal of Geophysical Research: Atmospheres*, *125*, 1–20. https://doi.org/10.1029/2020jd033579

Remsberg, E. E., Marshall, B. T., Garcia-Comas, M., Krueger, D., Lingenfelser, G. S., Martin-Torres, J., et al. (2008). Assessment of the quality of the Version 1.07 temperature-versus-pressure profiles of the middle atmosphere from TIMED/SABER. *Journal of Geophysical Research*, *113*(D17), D17101. https://doi.org/10.1029/2008JD010013

Robertson, D., Liddy, D., & Elford, W. (1953). Measurements of winds in the upper atmosphere by means of drifting meteor trails I. *Journal of Atmospheric and Terrestrial Physics*, *4*(4–5), 255–270. https://doi.org/10.1016/0021-9169(53)90059-2

Russell, J. M., III, Mlynczak, M. G., Gordley, L. L., Tansock, J. J., Jr., & Esplin, R. W. (1999). Overview of the SABER experiment and preliminary calibration results. In A. M. Larar (Ed.), *Opt. spectrosc. tech. instrum. atmos. sp. res. iii* (Vol. 3756, p. 277). https://doi.org/10.1117/12.366382

Salby, M. L. (1981). Rossby Normal modes in nonuniform background configurations. Part II. Equinox and solstice conditions. *Journal of the Atmospheric Sciences*, *38*(9), 1827–1840. https://doi.org/10.1175/1520-0469(1981)038<1827:RNMINB>2.0.CO;2

Salby, M. L., & Garcia, R. R. (1987). Vacillations Induced by Interference of Stationary and Traveling Planetary Waves. *Journal of the Atmospheric Sciences*, *44*(19), 2679–2711. https://doi.org/10.1175/1520-0469(1987)044<2679:VIBIOS>2.0.CO;2

Sandford, D. J., Beldon, C. L., Hibbins, R. E., & Mitchell, N. J. (2010). Dynamics of the Antarctic and Arctic mesosphere and lower thermosphere – Part 1: Mean winds. *Atmospheric Chemistry and Physics*, *10*(21), 10273–10289. https://doi.org/10.5194/acp-10-10273-2010

Sassi, F., Garcia, R. R., Boville, B. A., & Liu, H. (2002). On temperature inversions and the mesospheric surf zone. *Journal of Geophysical Research*, *107*(19), 4380. https://doi.org/10.1029/2001JD001525

Schoeberl, M., Douglass, A., Hilsenrath, E., Bhartia, P., Beer, R., Waters, J., et al. (2006). Overview of the EOS aura mission. *IEEE Transactions on Geoscience and Remote Sensing*, *44*(5), 1066–1074. https://doi.org/10.1109/TGRS.2005.861950

Shen, X., Wang, L., & Osprey, S. (2020a). The Southern Hemisphere sudden stratospheric warming of September 2019. *Scientific Bulletin*, *65*(21), 1800–1802. https://doi.org/10.1016/j.scib.2020.06.028

Shen, X., Wang, L., & Osprey, S. (2020b). Tropospheric forcing of the 2019 Antarctic sudden stratospheric warming. *Geophysical Research Letters*, *47*(20), 1–8. https://doi.org/10.1029/2020GL089343

Siskind, D. E., Coy, L., & Espy, P. (2005). Observations of stratospheric warmings and mesospheric coolings by the TIMED SABER instrument. *Geophysical Research Letters*, *32*(9), 1–4. https://doi.org/10.1029/2005GL022399

Smith, A. K. (1985). Wave transience and wave-mean flow interaction caused by the interference of stationary and traveling waves. *Journal of the Atmospheric Sciences*, *42*(6), 529–535. https://doi.org/10.1175/1520-0469(1985)042<0529:WTAWMF>2.0.CO;2

Smith, A. K. (1996). Longitudinal variations in mesospheric winds: Evidence for gravity wave filtering by planetary waves. *Journal of the Atmospheric Sciences*, *53*(8), 1156–1173. https://doi.org/10.1175/1520-0469(1996)053<1156:LVIMWE>2.0.CO;2

Teitelbaum, H., & Vial, F. (1991). On tidal variability induced by nonlinear interaction with planetary waves. *Journal of Geophysical Research*, *96*(A8), 14169–14178. https://doi.org/10.1029/91JA01019

Torrence, C., & Compo, G. P. (1998). A practical guide to wavelet analysis. *Bulletin of the American Meteorological Society*, *79*(1), 61–78. https://doi.org/10.1175/1520-0477(1998)079<0061:APGTWA>2.0.CO;2

Vial, F., Forbes, J. M., & Miyahara, S. (1991). Some transient aspects of tidal propagation. *Journal of Geophysical Research*, *96*(A2), 1215–1224. https://doi.org/10.1029/90ja02181

Wang, H., Boyd, J. P., & Akmaev, R. A. (2016). On computation of Hough functions. *Geoscientific Model Development*, *9*(4), 1477–1488. https://doi.org/10.5194/gmd-9-1477-2016

Waters, J., Froidevaux, L., Harwood, R., Jarnot, R., Pickett, H., Read, W., et al. (2006). The Earth observing system microwave limb sounder (EOS MLS) on the aura Satellite. *IEEE Transactions on Geoscience and Remote Sensing*, *44*(5), 1075–1092. https://doi.org/10.1109/TGRS.2006.873771

Yamazaki, Y. (2018). Quasi-6-day wave effects on the equatorial ionization anomaly over a solar cycle. *Journal of Geophysical Research: Space Physics*, *123*(11), 9881–9892. https://doi.org/10.1029/2018JA026014

Yamazaki, Y., & Matthias, V. (2019). Large-amplitude quasi-10-day waves in the middle atmosphere during final warmings. *Journal of Geophysical Research: Atmospheres*, *124*, 9874–9892. https://doi.org/10.1029/2019jd030634

Yamazaki, Y., Matthias, V., Miyoshi, Y., Stolle, C., Siddiqui, T., Kervalishvili, G., et al. (2020). September 2019 Antarctic sudden stratospheric warming: Quasi-6-day wave burst and ionospheric effects. *Geophysical Research Letters*, *47*(1), 1–12. https://doi.org/10.1029/2019GL086577

Yamazaki, Y., & Richmond, A. D. (2013). A theory of ionospheric response to upward-propagating tides: Electrodynamic effects and tidal mixing effects. *Journal of Geophysical Research: Space Physics*, *118*(9), 5891–5905. https://doi.org/10.1002/jgra.50487

Yee, J.-H., Cameron, G. E., & Kusnierkiewicz, D. Y. (1999). Overview of TIMED. In A. M. Larar (Ed.), *Opt. spectrosc. tech. instrum. atmos. sp. res. iii* (Vol. 3756, p. 244). https://doi.org/10.1117/12.366378

Yu, F. R., Huang, K. M., Zhang, S. D., Huang, C. M., Yi, F., Gong, Y., et al. (2019). Quasi 10- and 16-day wave activities observed through meteor radar and MST radar during stratospheric final warming in 2015 spring. *Journal of Geophysical Research: Atmospheres*, *124*, 6040–6056. https://doi.org/10.1029/2019JD030630

Yue, J., Wang, W., Richmond, A. D., Liu, H.-L., & Chang, L. C. (2013). Wavenumber broadening of the quasi 2 day planetary wave in the ionosphere. *Journal of Geophysical Research: Space Physics*, *118*(6), 3515–3526. https://doi.org/10.1002/jgra.50307